

Photoacoustic imaging of periorbital skin cancer *ex vivo*: unique spectral signatures of malignant melanoma, basal, and squamous cell carcinoma

MAGNE TORDENGREN STRIDH,^{1,*} JENNY HULT,¹  ABOMA MERDASA,¹  JOHN ALBINSSON,¹  AGNES PEKAR-LUKACS,² BODIL GESSLEIN,¹ ULF DAHLSTRAND,¹  KARL ENGELSBURG,¹ JOHANNA BERGGREN,¹ MAGNUS CINTHIO,³  RAFI SHEIKH,¹  AND MALIN MALMSJÖ¹

¹Ophthalmology, Department of Clinical Sciences Lund, Lund University, Skåne University Hospital, Lund, Sweden

²Department of Pathology, Skåne University Hospital, Lund, Sweden

³Department of Biomedical Engineering, Faculty of Engineering, Lund University, Sweden

*malin.malmsjo@med.lu.se

Abstract: Radical excision of periorbital skin tumors is difficult without sacrificing excessive healthy tissue. Photoacoustic (PA) imaging is an emerging non-invasive biomedical imaging modality that has potential for intraoperative micrographic control of surgical margins. This is the first study to assess the feasibility of PA imaging for the detection of periocular skin cancer. Eleven patients underwent surgical excision of periocular skin cancer, one of which was a malignant melanoma (MM), eight were basal cell carcinomas (BCCs), and two squamous cell carcinomas (SCCs). Six tumors were located in the eyelid, and five in periocular skin. The excised samples, as well as healthy eyelid samples, were scanned with PA imaging postoperatively, using 59 wavelengths in the range 680–970 nm, to generate 3D multispectral images. Spectral unmixing was performed using endmember spectra for oxygenated and deoxygenated Hb, melanin, and collagen, to identify the chromophore composition of tumors and healthy eyelid tissue. After PA scanning, the tumor samples were examined histopathologically using standard hematoxylin and eosin staining. The PA spectra of healthy eyelid tissue were dominated by melanin in the skin, oxygenated and deoxygenated hemoglobin in the orbicularis oculi muscle, and collagen in the tarsal plate. Multiwavelength 3D scanning provided spectral information on the three tumor types. The spectrum from the MM was primarily reconstructed by the endmember melanin, while the SCCs showed contributions primarily from melanin, but also HbR and collagen. BCCs showed contributions from all four endmembers with a predominance of HbO₂ and HbR. PA imaging may be used to distinguish different kinds of periocular skin tumors, paving the way for future intraoperative micrographic control.

© 2021 Optica Publishing Group under the terms of the [Optica Open Access Publishing Agreement](#)

1. Introduction

The most common periorbital skin cancers are malignant melanoma (MM), basal cell carcinoma (BCC) and squamous cell carcinoma (SCC). MM arises from melanocytes, and is the deadliest form of skin cancer overall [1]. BCC arises slowly *de novo* from the deepest layer of the epidermis. While BCC rarely metastasizes, it may cause devastating structural damage due to local invasion [2]. SCC originates from the keratinocytes and is characterized by a precursor stage of actinic keratosis. SCC tends to be locally aggressive with tissue destruction and perineural invasion, and is capable of orbital invasion [3].

Skin cancer is often diagnosed and treated simultaneously by excisional biopsy. Patients in which excision proves to be non-radical must undergo further surgery to completely remove the tumor. Since the main risk factor for developing skin cancer is exposure to UV light, the head, neck, and face are the most common locations [4], and 5% to 10% of all skin cancers occur on the eyelids [5]. Tumors in the head and neck area are often removed with a narrower margin to spare healthy tissue, reduce the extent of plastic surgical reconstruction, and to preserve the function of tissue. However, this increases the risk of non-radical excision. In a study on 1459 BCCs, Fleischer et al. found a 133% higher risk of making a nonradical excision of a tumor in the face and neck area than on the trunk [6]. This is especially true in the periocular area, as a defect eyelid exposes the cornea and rest of the eye, increasing risk of damage. [7–9].

Mohs micrographic surgery was developed for the intraoperative examination of tumor margins and radicality [10]. The tumor margins are examined by staged resection and simultaneous histopathological examination. Mohs surgery is considered the most efficient method for complete removal of high-risk skin tumors, and is particularly useful in regions where narrow margins are required. However, the procedure is time consuming, expensive, and dependent on the experience of the physician, which limits its use. A non-invasive method of determining tumor borders before or during surgical excision would thus be of considerable value.

Existing non-invasive methods of *in vivo* assessment of suspicious skin tumors include traditional dermoscopy, confocal microscopy, multiphoton microscopy, optical coherence tomography (OCT), Raman, fluorescence, and diffuse reflectance spectroscopy, and high-frequency ultrasound [11–18]. These methods are limited by either shallow imaging depth or lack of functional and molecular imaging capabilities [19]. In general, purely optical techniques can only probe a depth of a few millimeters into the tissue, at best. More importantly, none of these methods, except dermoscopy, has yet been established for clinical practice. Imaging methods providing true three-dimensional (3D) information from deep tissue layers, in real time, would enable physicians to plan the surgical procedure more efficiently resulting in more precise excisions with adequate margins, lower relapse rates, and a more available ways of examining tumor radicality in Mohs micrographic surgery. One such method is 3D LC-OCT (*deepLive* by Damae Medical) which provides highly resolved 3D images: although the depth is still only limited to less than a millimeter, such a probing depth might be sufficient in the framework of most skin cancers diagnosis.

PA imaging is currently one of the most rapidly developing non-invasive biomedical imaging tools [20]. It is a hybrid imaging technology that produces high-resolution images by combining ultrasonic and optical imaging to reveal the molecular composition of tissues at high resolution. The tissue is irradiated with non-ionizing nanosecond laser light pulses of different wavelengths. The energy from the light is absorbed differently by different tissue chromophores, inducing so-called thermoelastic expansion. This generates ultrasonic waves that can be detected by an ultrasonic transducer. Spectra are obtained from the tissue that can be converted into multispectral 2D and 3D chromophore-specific images using so-called linear spectral unmixing, henceforth called only spectral unmixing or SU. The detection of small variations in tissue composition using PA is thus superior to that possible with other methods.

So far, PA imaging has mainly been developed for experimental use [21]. Only a few studies have been performed on human skin cancer, most of which were on melanotic skin tumors [22–35], and only few on non-melanotic skin tumors [20,35,36]. We recently reported a case of BCC, in which PA imaging was suggested as an alternative technique for intraoperative micrographic control of the surgical margins on the eyelid [37]. Apart from this, no other studies have been performed on the feasibility of using PA imaging for periocular tumor margin.

The aim of the present study was to identify the spectral signatures of periocular MM, BCC and SCC, and to investigate how these differ from that of healthy tissue, using PA imaging on excised lesions *ex vivo*. 3D multiwavelength PA scanning was performed using 59 excitation wavelengths

from 680 nm to 970 nm. The absorption of the different tumor types was analyzed regarding chromophore composition, using spectral unmixing, taking the absorption of oxygenated and deoxygenated hemoglobin melanin, and collagen into consideration. This is a critical step in the development of PA imaging for the non-invasive detection of tumor borders in the clinical setting. However, PA imaging in the present study was limited to *ex vivo* acquisitions.

2. Materials and methods

2.1. Ethics

The experimental protocol for this study was approved by the Ethics Committee at Lund University, Sweden. The research was performed according to the 2008 Declaration of Helsinki. The participants were given both verbal and written information about the study and its voluntary nature. Written consent was obtained from all participants.

2.2. Patient inclusion

Patients were recruited from the Department of Dermatology at Skåne University Hospital in Lund, between June 2019 and May 2021 for *ex vivo* investigation of their lesions. The inclusion criteria were: age ≥ 18 years, skin tumor in the periocular region in need of surgical excision, and tumor size smaller than 20×20 mm. The size of the tumor was limited by the size of the probe in the PA equipment. Patient characteristics are given in Table 1.

2.3. Sample preparation and examination

The tumors were excised under local anesthesia by surgeons at the Department of Ophthalmology in Lund, placed in an isotonic saline solution and transported to a laboratory next door. Any hair was cut off from the samples before scanning. The samples were then mounted in saline in a $100 \times 70 \times 50$ mm custom-made Plexiglas container using 1-2 Prolene 6-0 sutures (Ethicon, Bridgewater, NJ, USA) at each end of the lesion, as described previously [38]. A 10 mm thick Aquaflex ultrasound gel pad (Parker Laboratories Inc., Fairfield, CT, USA), covered with a plastic film, was used to achieve a suitable distance between the PA probe and the skin line. A layer of black ultrasound-attenuating material was placed in the bottom of the container. After PA imaging, the excised skin samples were placed in formaldehyde and sent for histopathological examination.

2.4. Photoacoustic imaging

PA imaging was performed using a Vevo LAZR-X system (FUJIFILM VisualSonics Inc., Toronto, ON, Canada), which employs a laser source with spectrally tunable nanosecond laser pulses for excitation and ultra-high-frequency ultrasound for detection. The linear ultrasound transducer (MX400) has a central frequency of 30 MHz and a bandwidth of 20–46 MHz. The effective axial and lateral resolutions are $50 \mu\text{m}$ and $110 \mu\text{m}$, respectively, and the image width is 512 pixels, while the height varied between 600–700 pixels, depending on the signal strength. The diagnostic ultrasound scans are interleaved with laser pulses at a repetition rate of 20 Hz. Fifty-nine excitation wavelengths were used between 680–970 nm (in steps of 5 nm) to produce a multispectral PA image (Fig. 1(a)). The laser pulses are guided via a fiberoptic bundle to generate two planar light beams aligned parallel to the linear ultrasound transducer at the skin surface.

The PA transducer was attached to a linear stepper motor (VisualSonics Inc.) allowing the lesion to be scanned in steps of 0.5 mm to obtain a sequence of multispectral PA images, from which a 3D image of the lesion could be generated during post-processing. This was accomplished by combining either a US or PA image of a specific wavelength from each location along the acquisition path of the sample into a stack of images, forming a three-dimensional matrix. The stepper motor was attached to an adjustable arm (Mounting Accessory, GCX Corporation,

Table 1. Patient characteristics and histopathological characteristics of tumors. Skin type is defined as Fitzpatrick skin type (1-6).^a

Tumor specimen	Age	Sex	Smoker	Skin type	Type	Eyelid	Location	Radical	Type of excision	Width (mm)	Depth (mm)
MM1	77	F	No	2	In situ	Inferior	Central	No	Wedge	Non-radical*	0.3
SCC1	73	M	Yes	2	In situ	Superior	Cranial	Yes	Skin only	9.1	2.2
SCC2	55	M	No	1	In situ	Inferior	Caudal	Yes	Skin only	4.3	0.2
BCC1	53	M	No	3	Nodular	Inferior	Temporal	Yes	Skin only	5.6	2.2
BCC2	47	F	No	1	Nodular	Superior	Temporal	Yes	Skin only	3.9	2.9
BCC3	60	F	Yes	1	Infiltrative	Superior	Central	Yes	Wedge	2.5	0.9
BCC4	70	F	Yes	1	Infiltrative	Canthus	Nasal	Yes	Skin only	3.4	0.9
BCC5	74	M	No	3	Morphea-like	Inferior	Nasal	Yes	Skin only	14.4	3.7
BCC6	71	M	No		Infiltrative	Inferior	Central	No	Wedge	Non-radical*	3.4
BCC7	69	F	No	2	Infiltrative	Inferior	Temporal	Yes	Wedge	5.1	1.9
BCC8	76	M	No	3	Not specified	Inferior	Central	Yes	Wedge	8.1	1.3

^aTumor width is unknown since the excision is non-radical

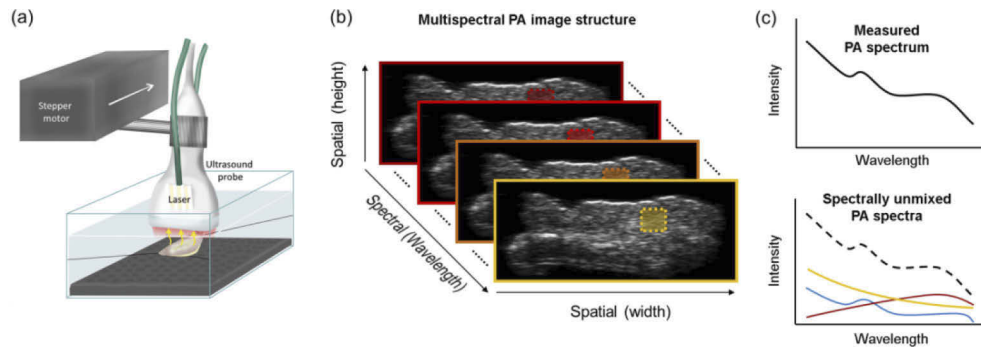


Fig. 1. (a) Schematic illustration showing the photoacoustic examination setup. The photoacoustic probe consists of an ultrasound probe with laser fiberoptic bundles attached. The tumor is irradiated with pulsed laser light causing thermoelastic expansion, which in turn generates acoustic waves that can be detected by an ultrahigh-frequency ultrasound scanner. The probe is attached to an adjustable arm with a linear stepper motor to obtain 2D images with a step size of 500 μm for the reconstruction of 3D images. (b) Illustration of the data structure of a multispectral PA image. A PA image is recorded at each excitation wavelength, together with an ultrasound image of the same cross-section. A multispectral image therefore consists of 59 individual PA images, each obtained at a unique excitation wavelength. The region of interest indicated by the dashed square is located at the same position in all PA images, from which individual spectra are extracted. (c) Once a single spectrum is obtained, spectral unmixing is performed to decompose it into a linear combination of known, so-called endmember spectra representing different chromophores (the colored traces). Note that the spectra are schematically drawn and do not represent actual data.

Petaluma, CA, USA) to remove motion artifacts introduced by hand-held operation. The PA probe is 21 mm wide and enables scanning of tumors up to 14 mm in diameter.

2.5. Data processing and spectral unmixing

Raw data were exported from the VisualSonics Vevo LAB 3.1.0 software and imported into MATLAB R2017b (MathWorks Inc., Natick, MA, USA) where all the analysis was performed. The data were preprocessed to automatically remove signals from the ultrasound gel, plastic film, and the saline solution, as outlined by Hult et al [38]. The PA spectra were extracted on a pixel-by-pixel basis. Regions of interest (ROIs) were carefully selected in tumor and healthy tissue PA spectra from adjoining pixels within each ROI were spatially averaged to produce a single spectrum for further analysis (Fig. 1(a)). As the PA signal varies between patients, the data must be normalized to allow comparison. This was achieved by dividing both the PA spectra from tumor and healthy tissue by the spectrally averaged PA signal acquired from the healthy tissue spectrum. Tumor spectra are thus always represented in relation to healthy tissue spectra, which should minimize patient-to-patient variation.

Spectral unmixing was performed to identify the chromophores most likely to be responsible for the measured PA spectrum. The measured PA spectrum is decomposed into a linear combination of so-called endmember spectra that represent chromophores with known absorption features (Fig. 1(b)). In the present study, it was assumed that the most dominant absorbers were oxygenated and deoxygenated hemoglobin (HbO_2 and HbR), melanin, and collagen, and the absorption spectra were used as found in [39,40]. Water absorption was initially accounted for in the spectral unmixing analysis, but was later omitted since it caused a rather weak imprint on the PA spectrum of tissue, due to its comparatively low absorption coefficient [39]. Elastin has similar absorption features to collagen [41], and was therefore excluded as an endmember in

order to reduce redundancy. A non-negative matrix factorization algorithm ('lsqnonneg.m') that constrains the linear coefficients of the endmembers to zero or positive values was used for spectral unmixing. A detailed description of the spectral unmixing approach has been given previously [40].

Spectral unmixing is often used to perform quantitative analysis when the concentration of a particular endmember is required. However, due to spectral coloring [42] and the difficulty in determining how many photons produce a particular PA response [43] no quantitative analysis was performed in this study. Rather, the focus was on differences in endmember abundance between tumors and healthy tissue in the eyelid. The endmember contribution is therefore presented as a fraction (%) of the measured signal.

2.6. Laser safety

Laser and ultrasound safety must be taken into consideration when using a PA imaging system. PA examinations were performed as described previously [44]. The windows of the examination room were covered with matt black aluminum foil, and the doorway was covered with a blackout curtain to prevent laser light from leaving the room. To minimize the risk of eye injuries, protective eye shields, in combination with aluminum foil, were worn by the study subjects throughout the examination. Block-out glasses were worn by the staff. In previous studies in the temples region we have shown that the laser radiant exposure and the ultrasound power to which the subjects were exposed, are well below the laser safety levels given in IEC 60825-1 [45] and the ultrasound safety level required by the FDA [46] and the British Medical Ultrasound Society [44,47]. The present study was performed *ex vivo* on excised samples and thus laser radiant exposure does not pose a problem to the patient.

2.7. Histopathological examination

After *ex vivo* PA imaging, the lesion was placed in formalin and sent for histopathological examination using standard sectioning and staining with hematoxylin and eosin. The sections were scanned using Sectra IDS7 software to provide digital images (Sectra AB, Linköping, Sweden), and were analyzed by an experienced pathologist (A.P.). The tumor type was diagnosed, and the tumor borders were delineated, as were the healthy structures of the eyelid, including the skin, orbicularis oculi muscle, and tarsal plate.

When comparing PA images to histological cross-sections it is non-trivial to identify the exact location, for a number of reasons. Firstly, the histological cross-sections are a few μm thick, while the PA images probe a tissue thickness that is almost two orders of magnitude greater. Secondly, acquiring comparable images would require the pathologist to slice the sample exactly perpendicular to the direction of the PA measurement. Finally, the sample is fixed in formalin prior to histopathological analysis, causing it to shrink. It is therefore difficult to identify the exact same locations in the two imaging methods, and we therefore focused on identifying regions that contained the tumor or healthy tissue.

2.8. Statistical analysis

As the data included only one MM and two SCCs, these results could not be analyzed on group basis. BCCs were found in 8 patients, and the results for these are expressed as mean values \pm SD. Statistical analysis was performed using paired two-way ANOVA with Šidák correction for multiple comparisons. Significance was defined as $p \leq 0.05$.

2.9. Patient and histological characteristics

All patients were of paler skin types (Fitzpatrick I-III). Histological sectioning was used to identify tumor type and growth pattern. The MM and SCCs were *in situ*, whereas BCC subtypes varied between nodular and infiltrative tumors. Six tumors were located on the upper and lower

eyelids, and five were located on the surrounding periocular skin. Only two tumors were >10 mm in lateral width, and only one exceeded 3 mm in depth. (See Table 1 for details.)

3. Results

3.1. Healthy eyelids

The anatomical structures of the eyelid, including the skin, orbicularis oculi muscle, and tarsal plate, were identified in the histological sections from tumors excised with wedge resection ($n=5$) (Fig. 2(a)). Spectral information was retrieved from the same locations in the corresponding ultrasound (Fig. 2(b)) and PA images (Figs. 2(c)). A clear difference was seen between the PA spectral signatures in the skin, orbicularis muscle, and tarsal plate (Fig. 2(d)). Linear spectral unmixing, using endmember absorption spectra from HbO_2 , HbR, melanin and collagen, revealed differences in the endogenous chromophore distribution between the skin, (dominated by melanin), the orbicularis muscle (dominated by hemoglobin) and the tarsal plate (dominated by collagen) (Fig. 2(e)).

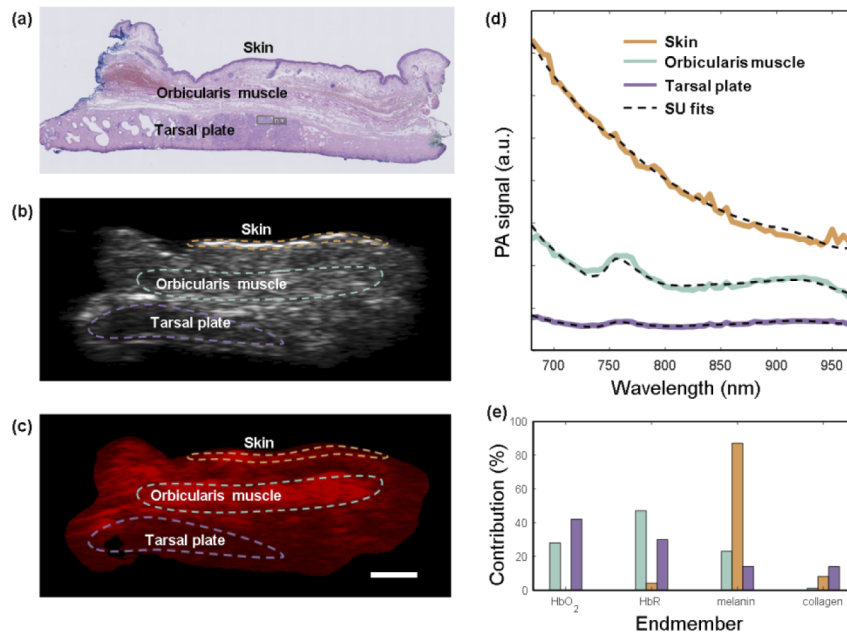


Fig. 2. (a) Histological cross section of a healthy eyelid in which the anatomical structures are identified. Corresponding ultrasound (b) and PA images (c) of the same eyelid, showing the regions of interest used when analyzing the spectral signatures. Scale bar = 2 mm. (d) The PA spectra obtained for the skin (orange), orbicularis muscle (turquoise), and tarsal plate (purple). The dashed curves show the fits obtained from spectral unmixing (SU). The coefficient of determination was $R^2 > 0.85$ for all tumors, indicating a strong fit of the data using these four endmembers. (e) The relative contributions of the endmembers for HbO_2 , HbR, melanin, and collagen to the PA spectra of the eyelid structures obtained by spectral unmixing. Note the predominance of melanin in the skin, hemoglobin in the muscle, and collagen in the tarsal plate.

3.2. PA tumor spectra

The tumors were identified by histopathological examination, and the tumor spectrum was obtained from the corresponding location in the PA image, and compared to that of the surrounding healthy

tissue. A clear difference was seen between the intensity of the PA signal in the MM and the surrounding healthy tissue, almost an order of magnitude (Fig. 3). The 8 BCCs were analyzed on group level. A significant difference ($p < 0.0001$) was found between the BCCs and healthy tissue when comparing PA signal over the entire spectral range from 680 to 970 nm with paired two-way ANOVA. The Šidák correction test for multiple comparisons was used to compare PA signal at individual wavelengths, and showed a significant difference between tumor and healthy tissue for all wavelengths between 680 and 795 nm ($p < 0.05$). The spectral signatures of the two confirmed SCC tumors differed markedly, probably due to cellular differences between them. Both were SCCs *in situ*, but one was combined with actinic keratosis, while the other showed a strongly hyper-parakeratinized papillomatous growth pattern. Since the two SCC samples were from two tumors with distinctly different compositions, the SCC *in situ* with actinic keratosis was chosen for analysis.

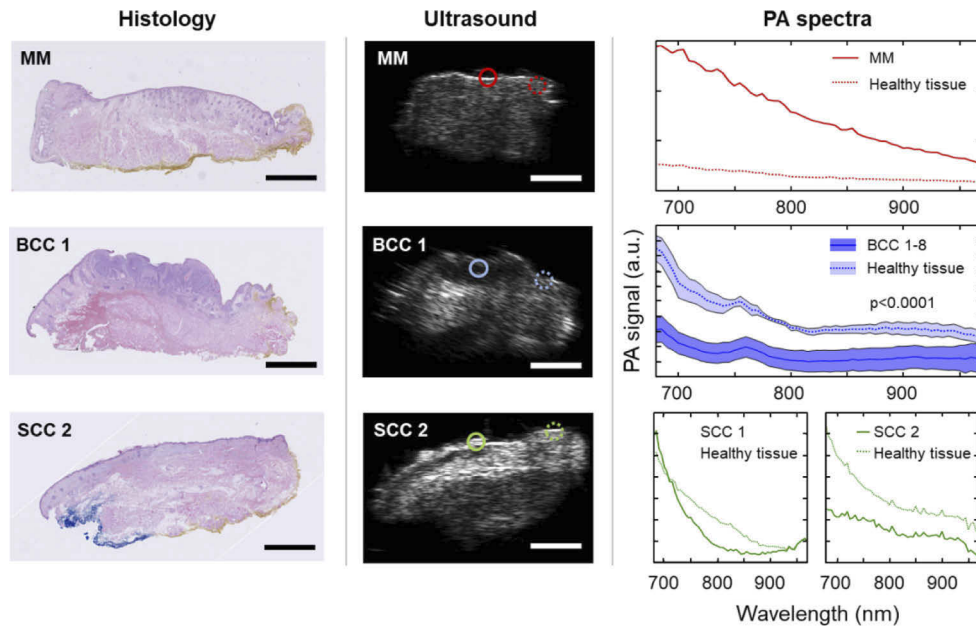


Fig. 3. Histological sections (left column) of a malignant melanoma (MM), a squamous cell carcinoma (SCC 2) and a basal cell carcinoma (BCC 1) and the corresponding ultrasound images (middle column), in which the regions of interest in the center of the tumor (solid line) and in healthy tissue (dotted line) are shown. The right-hand column shows the results of analysis of the PA signal. Spectral information was obtained from one MM, two SCCs, and 8 BCCs (MM and SCC data are shown individually, whereas BCC data is shown as the mean \pm SD). Statistical comparison between tumor and healthy tissue was performed using paired two-way ANOVA. Scale bars = 2 mm.

3.3. Spectral unmixing of the tumor spectra

Spectral unmixing was used to further investigate the origin of the spectral changes observed in the three types of tumor (Fig. 4). The MM tumor spectrum can be completely reconstructed by the absorption by melanin, which is confirmed by the visible pigmented regions in the color photograph. The spectrum from the BCCs was reconstructed by a combination of all four endmembers, although the absorption from HbO₂ and HbR was most notable. The spectrum from the SCCs also shows substantial contributions from two endmembers, although, in contrast to BCC, melanin is the dominating endmember.

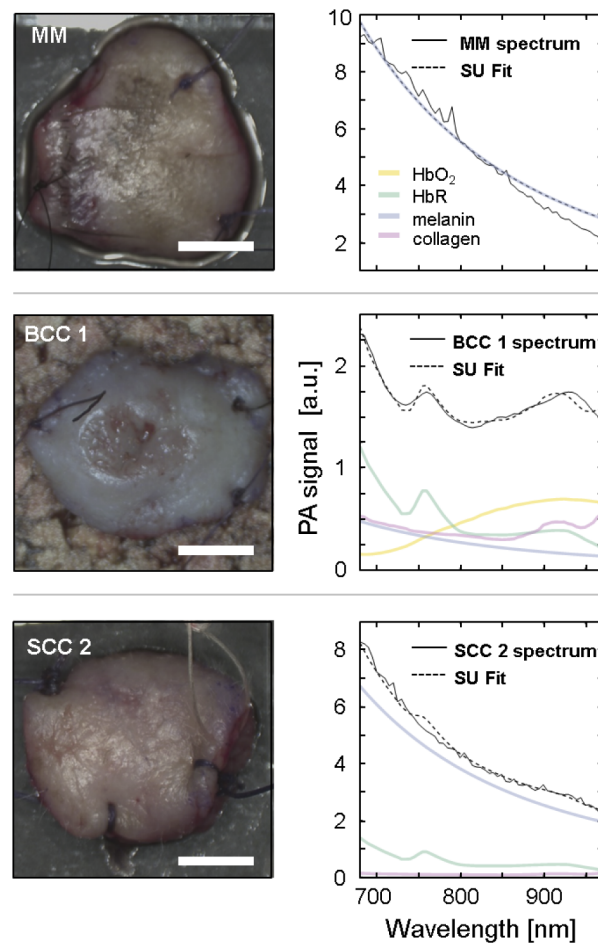


Fig. 4. Photographs of the malignant melanoma (MM in Table 1), a squamous cell carcinoma (SCC 2) and a basal cell carcinoma (BCC 1) and their corresponding PA spectra. Spectral unmixing was performed using endmember spectra for HbO₂, HbR, melanin, and collagen. The solid black lines are from the tumor and the dashed black lines the fit from spectral unmixing. The coefficient of determination was $R^2 > 0.95$ for all tumors, indicating a good fit to the data using these four endmembers. Scale bars = 5 mm.

3.4. Comparison of tumor composition to that of healthy tissue

Detailed comparisons were made of the endmember contributions in the tumors and healthy tissue (Fig. 5). For the MM, the most notable difference is a reduction in collagen together with an increase in melanin, while the contributions from HbO₂ and HbR is negligible. BCC 1 showed a distinct increase in HbO₂, and a decrease in HbR, compared to healthy tissue. This suggests increased vascularization of the tumor, and a change in the oxygenation. A small decrease in collagen was also seen. SCC 2 showed a slight increase in melanin and a decrease in collagen, similar characteristics to MM. Additionally, a more pronounced decrease in HbR was seen in SCC 2.

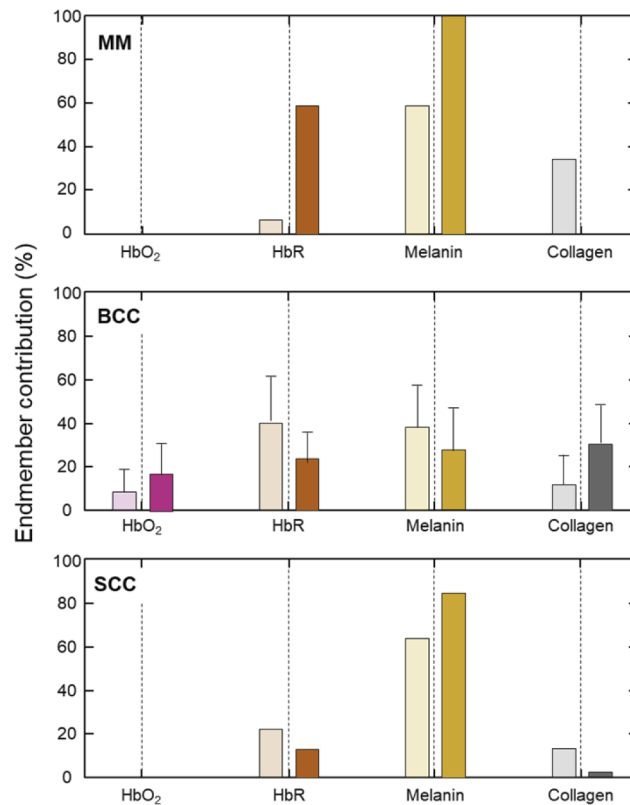


Fig. 5. Endmember contributions in tumors (dark colors) compared to healthy tissue (pale colors) obtained by linear spectral unmixing assuming the presence of endmember absorption spectra from HbO₂, HbR, melanin, and collagen, highlighting the key spectral differences for MM (top), BCC (middle, BCC 1-8) and SCC (bottom, SCC 2). The results for the 8 BCCs are shown as the mean \pm SD. Statistical analysis was performed using paired two-way ANOVA, which indicated significant differences when comparing all endmembers in the tumors versus healthy tissue ($p = 0.0348$). Šidák correction for multiple comparisons was performed to enable analysis of the individual endmembers, and the p -values were determined to be 0.218, 0.011*, 0.319, and 0.113 for HbO₂, HbR, melanin, and collagen, respectively.

4. Discussion

The findings of the present study show that PA imaging can be used to obtain distinct absorption patterns for MM, BCC and SCC that reflect the molecular composition of the tumors. To the best of the authors' knowledge this is the first time PA imaging has been used to compare the spectral signatures of these three tumor types in the periorbital region. Furthermore, this study is distinct from previous studies in that spectral analysis was performed over a broad wavelength range (59 wavelengths between 680 and 970) in three dimensions.

4.1. MM spectrum

The results for the MM show that absorption was stronger in the tumor than in the surrounding healthy tissue. MM is the result of the proliferation of melanocytes in the epidermis that produce melanin, an endogenous chromophore showing strong light absorption in the range 600 to 1000 nm. Indeed, spectral unmixing of the PA data from the MM revealed a particularly

good fit to melanin (~100%), while the contributions from other tissue chromophores were not measurable, although they are likely to be present at low concentrations. Although our results come from only one MM sample, they are in line with the little data available from the few previous studies on PA imaging of melanomas in humans on other parts of the body, in which a limited number of wavelengths were used. Breathnach et al. examined 6 melanomas *in vivo* using PA imaging at 5 excitation wavelengths (680, 700, 750, 850, and 900 nm) [30]. In a similar study, Park et al. examined 5 melanomas with PA imaging *in vivo*, also using 5 wavelengths (700, 756, 796, 866 and 900) [48], while Kim et al. used 3 excitation wavelengths (680, 800 and 1064 nm) to examine one *in situ* human melanoma *ex vivo* [34]. Finally, Zhou et al. examined 10 melanomas *ex vivo* using only one wavelength (680 nm) [32].

In the present study, a large number of wavelengths (59) was used over a broader spectral range (680–970 nm), to provide more detailed information on the molecular composition of the tissue, increasing the probability of identifying differences between tumor and healthy tissue. In a recent study on 52 melanomas [49], our group was able to show that more excitation wavelengths allowed for more robust spectral unmixing analysis, providing a more detailed map of the distribution of tumor cells, compared to using only a few wavelengths. This is a distinct improvement on the previous studies mentioned above, in which tumor borders were defined only by high absorption amplitudes or by the PA absorption signal of melanin alone. Furthermore, the results of the present study also show a lesser collagen component in MM than in healthy tissue, which could be used to strengthen the identification of melanomas. Collagen absorption peaks have been studied by Park et al. in the short-wave infrared spectral range (SWIR, 1100–2000nm) [48]. Collagen absorption in the near-infrared spectral range is overshadowed by that of oxygenated and deoxygenated blood, as well as melanin. However, light absorption by water increases significantly in the SWIR spectral range, which limits the penetration depth, making it less suitable for multispectral analysis of other tissue components.

4.2. BCC spectrum

In contrast to MM, the absorption of SCCs and BCCs was lower than that of the surrounding healthy tissue, indicating a possible means of differentiating between melanotic and non-melanotic lesions using PA imaging. So far, only two other research groups have used PA imaging to study BCCs [20,35,36,50]. A research group at the National Skin Center in Singapore has shown that PA imaging could be used to visualize BCCs in a small group of 26 patients [31]). They performed 3D reconstructions using 10 wavelengths between 700 and 900 nm [27,31]. However, the majority of the patients in their study had pigmented BCCs, and the tumors were defined by their melanin signals after spectral unmixing. While pigmentation of BCCs is seen in 50% of the Black, Hispanic, and Japanese populations, only 6% of BCCs are pigmented in Caucasians [51]. Our recent study of non-periocular BCCs was on a Caucasian population [37], and, as in the present study, the patients had paler skin (Fitzpatrick skin type I-III in the present study), and none had a pigmented lesion. Indeed, the results of the present study showed that melanin made a low contribution to the spectral signal in the BCCs, confirming that BCC tumor identification cannot be based on melanin absorption alone.

Hemoglobin is a strong endogenous chromophore, both in its oxygenated and deoxygenated state, with absorption in the wavelength range 680–970 nm [52]. Spectral unmixing of the spectra from the BCCs in the present study revealed higher fractions of HbO₂ compared to normal tissue, with a distinct peak in oxygenated blood which may be explained by tumor angiogenesis. Like all tissues, tumors require sustenance in the form of nutrients and oxygen, as well as the ability to evacuate metabolic waste and carbon dioxide. Cells in a low-oxygen state can recruit new blood vessels by producing vascular endothelial growth factor hormone. This results in a tumor where increasing size induces equally increasing blood supply [34,48]. Indeed, arborizing blood vessels are a clinical hallmark of BCC [53]. We therefore suggest that the absorption of HbO₂

and HbR be included in spectral analysis for the diagnosis of BCC in the future, as this may reveal tumor-specific vasculature.

The spectral signature of a tumor reflects its molecular composition. The cellular origin of BCC has not been completely elucidated, but it has been reported that BCC can arise from multiple epidermal and follicular compartments [54,55]. Cytokeratin is expressed in all types of epithelial cells, and is often used as an immunohistological marker for non-melanoma skin tumors [54,56]. These cellular features may explain the differences between the spectra from BCC and healthy tissue.

4.3. SCC spectrum

We have recently demonstrated the use of multispectral PA imaging on non-periocular SCC, where SCC was successfully differentiated from healthy tissue in the wavelength range 765–960 nm [32]. In the present study, we performed a more extensive spectral analysis of chromophore absorption. Two specimens of SCC *in situ* were analyzed, one combined with actinic keratosis and the other with a hyper-parakeratinized papillomatous growth pattern. The spectral signal of the two tumors differed, reflecting their different cellular composition. One hallmark of cutaneous SCC is the increased amount of proliferating keratinocytes, and keratin is often used as an immunobiological marker in histopathological analysis [54,56]. However, keratin absorbs light mainly in the ultraviolet region [57], which is not suitable for PA imaging due to its potentially harmful photochemical effect, as well as its short penetration depth in tissue.

Other distinct chromophore patterns in both SCCs compared to healthy tissue, were the strong melanin absorption, and the weakened signal from collagen. The higher melanin content can be explained by proliferating keratinocytes, which, when exposed to UV light, cause the melanocytes to increase melanin production, providing protection from UV exposure [58]. A low collagen signal may be explained by tumor heterogeneity, as SCC tumors display a wide range of tumor variants with different appearances.

4.4. Eyelid composition

The use of PA imaging in the eyelid is especially challenging as eyelids consist of several components with different spectroscopic features, as reported in one of our previous studies on eyelid tissue excised during entropion repair [37]. In the present study, we performed more detailed spectral unmixing, revealing more information on endmember contribution to the spectral signal. This and the endmember contributions reflected the known constituents of the respective structures. The well-perfused orbicularis muscle showed a high amount of hemoglobin, the tarsal plate was characterized by collagen, while the spectrum from skin was dominated by the strongly adsorbing endogenous chromophore melanin. Knowledge of the PA signal from the normal eyelid will facilitate the detection of the subtle differences in the chromophore composition of tumors. This may be particularly important for non-pigmented BCC and SCC, as the PA signals from these tumors differ less from that of normal healthy tissue, than in the case of malignant melanomas.

4.5. Limitations

The clinical use of PA imaging in the periocular region is currently limited due to the high energy of the laser. It may be possible to use the technique in this area in the future, provided the energy levels are closely regulated, and the retina is protected from laser radiation, provided the safety aspects are carefully considered and evaluated. The pigment cells of the retina absorb light in the wavelength range 680–970 nm, which may lead to the risk of burns when using this technique. However, the focusing of the incoming PA laser light by the lens and cornea may be most harmful, but it may be sufficient to perform PA imaging with the eye closed, using low energy levels. We recently investigated PA imaging in the region of the temple, using visual acuity, color vision,

or visual field testing before and after examination, without detecting any harmful effects [59]. Until the possible risks of *in vivo* imaging have been thoroughly investigated, PA imaging can be used to image freshly excised, unfixed tumor samples during surgery. This will allow rapid intraoperative examination to determine whether the excision is radical, or if further excision is necessary, saving time compared to conventional microscopic histological examination, as in Mohs micrographic surgery.

The present study was limited by the sample size. Variability was seen in both the spectra from the two SCCs as well as in the group of BCCs. Different subtypes of cutaneous SCCs have unique histopathological features, and variations in the PA signals could therefore be expected. Further studies are required on larger groups of histologically different tumors to investigate whether it is possible to differentiate between subtypes based on their spectra.

Another limitation was that PA imaging was only performed on surgically excised tumors. This meant that the examination environment was free from motion artifacts, resulting in high-resolution spectra. We are currently developing a motion tracking system to allow detailed high-resolution images to be obtained *in vivo* [60].

A major limitation in current PA imaging technology is that light is increasingly attenuated with tissue depth, and the degree of attenuation at each wavelength depends on the tissue type [30]. This phenomenon is called spectral coloring and occurs as incident photons successively penetrate deeper into the tissue and experience wavelength-dependent absorption in different tissue layers, which may affect the spectral analysis. Various post-processing refinement approaches have been suggested [34,48], but these methods must be refined if we are to be able to reliably determine tumor depth *in vivo*.

5. Conclusion

PA imaging has considerable potential for translation into the clinical setting as it allows non-invasive molecular imaging at high resolution (axial and lateral resolutions of 50 μm and 110 μm) at sufficient imaging depths for skin cancer. In this study, we have demonstrated the feasibility of PA imaging in the most common forms of periocular tumors. Detailed spectral information was acquired over a broad wavelength range (680–970 nm) allowing detailed spectral analysis for the discrimination of tumor and healthy tissue. Distinct spectral signatures were observed, namely, high melanin absorption in MM, high signals from HbR and collagen in BCC, and a weak component from collagen together with a strong melanin component in SCC. These features can be used to discriminate tumors from normal periocular structures which show a prevalence of melanin in the skin, hemoglobin in the orbital muscle and collagen in the tarsal plate. These results contribute to the rapidly developing knowledge on PA imaging, and will be useful in designing future studies, with the ultimate goal of intraoperative micrographic control of the surgical margins of periocular tumors.

Funding. Swedish Government Grant for Clinical Research; Skåne University Hospital (SUS) Research Grants; Skåne County Council's Research and Development Foundation; Lund University Grant for Research Infrastructure; Swedish Cancer Foundation; Crown Princess Margaret's Foundation; Friends of the Visually Impaired Association in the county of Gävleborg; Stiftelsen för Synskadade i f.d. Malmöhus län; Lund Laser Center Research Grant; Carmen and Bertil Regnér's Foundation; IngaBritt och Arne Lundbergs Forskningsstiftelse; Cronqvist Foundation; Swedish Medical Association and Lund University grant for Research Infrastructure.

Acknowledgements. We would particularly like to thank Helen Sheppard for her valuable help with the language. We would also like to thank all the surgical staff involved at the Department of Ophthalmology.

Disclosures. The authors declare no conflicts of interest.

Data availability. Data underlying the results presented in this paper are not publicly available at this time but may be obtained from the authors upon reasonable request.

References

1. D. Schadendorf, A. C. J. van Akkooi, C. Berking, K. G. Griewank, R. Gutzmer, A. Hauschild, A. Stang, A. Roesch, and S. Ugurel, "Melanoma," *Lancet* **392**(10151), 971–984 (2018).
2. S. Ugurel, J. Rohmel, P. A. Ascierto, J. C. Becker, K. T. Flaherty, J. J. Grob, A. Hauschild, J. Larkin, E. Livingstone, G. V. Long, P. Lorigan, G. A. McArthur, A. Ribas, C. Robert, L. Zimmer, D. Schadendorf, and C. Garbe, "Survival of patients with advanced metastatic melanoma: The impact of MAP kinase pathway inhibition and immune checkpoint inhibition - Update 2019," *European Journal of Cancer* **130**, 126–138 (2020).
3. M. Rastrelli, S. Tropea, C. R. Rossi, and M. Alaibac, "Melanoma: epidemiology, risk factors, pathogenesis, diagnosis and classification," *In Vivo* **28**, 1005–1011 (2014).
4. C. Garbe, T. Amaral, K. Peris, A. Hauschild, P. Arenberger, L. Bastholt, V. Bataille, V. Del Marmol, B. Dreno, M. C. Fargnoli, J. J. Grob, C. Holler, R. Kaufmann, A. Lallas, C. Lebbe, J. Malvehy, M. Middleton, D. Moreno-Ramirez, G. Pellacani, P. Saiag, A. J. Stratigos, R. Vieira, I. Zalaudek, A. M. M. Eggermont, and t. E. A. o. D.-O. European Dermatology Forum, R. the European Organization for, and C. Treatment of, "European consensus-based interdisciplinary guideline for melanoma. Part 2: Treatment - Update 2019," *European Journal of Cancer* **126**, 159–177 (2020).
5. A. N. Crowson, C. Magro, and M. C. Mihm Jr., "Unusual histologic and clinical variants of melanoma: implications for therapy," *Curr Oncol Rep* **9**(5), 403–410 (2007).
6. C. G. Ethun and K. A. Delman, "The importance of surgical margins in melanoma," *J. Surg. Oncol.* **113**(3), 339–345 (2016).
7. J. C. Ng, S. Swain, J. P. Dowling, R. Wolfe, P. Simpson, and J. W. Kelly, "The impact of partial biopsy on histopathologic diagnosis of cutaneous melanoma: experience of an Australian tertiary referral service," *Arch Dermatol* **146**, 234–239 (2010).
8. V. H. Stell, H. J. Norton, K. S. Smith, J. C. Salo, and R. L. White Jr., "Method of biopsy and incidence of positive margins in primary melanoma," *Ann Surg Oncol* **14**(2), 893–898 (2007).
9. D. J. Karimipour, J. L. Schwartz, T. S. Wang, C. K. Bichakjian, J. S. Orringer, A. L. King, C. C. Huang, and T. M. Johnson, "Microstaging accuracy after subtotal incisional biopsy of cutaneous melanoma," *J Am Acad Dermatol* **52**(5), 798–802 (2005).
10. K. A. Prickett and M. L. Ramsey, "Mohs Micrographic Surgery," in *StatPearls* (StatPearls Publishing, 2021).
11. C. Benvenuto-Andrade, S. W. Dusza, A. L. Agero, A. Scope, M. Rajadhyaksha, A. C. Halpern, and A. A. Marghoob, "Differences between polarized light dermoscopy and immersion contact dermoscopy for the evaluation of skin lesions," *Arch Dermatol* **143**(3), 329–338 (2007).
12. E. Dimitrow, M. Ziemer, M. J. Koehler, J. Norgauer, K. Konig, P. Elsner, and M. Kaatz, "Sensitivity and specificity of multiphoton laser tomography for in vivo and ex vivo diagnosis of malignant melanoma," *J Invest Dermatol* **129**(7), 1752–1758 (2009).
13. T. Gambichler, P. Regeniter, F. G. Bechara, A. Orlikov, R. Vasa, G. Moussa, M. Stucker, P. Altmeyer, and K. Hoffmann, "Characterization of benign and malignant melanocytic skin lesions using optical coherence tomography in vivo," *J Am Acad Dermatol* **57**(4), 629–637 (2007).
14. W. Dummer, H. J. Blaheta, B. C. Bastian, T. Schenk, E. V. Brocker, and W. Remy, "Preoperative characterization of pigmented skin lesions by epiluminescence microscopy and high-frequency ultrasound," *Arch Dermatol* **131**(3), 279–285 (1995).
15. L. Lim, B. Nichols, M. R. Migden, N. Rajaram, J. S. Reichenberg, M. K. Markey, M. I. Ross, and J. W. Tunnell, "Clinical study of noninvasive in vivo melanoma and nonmelanoma skin cancers using multimodal spectral diagnosis," *J. Biomed. Opt* **19**(11), 117003 (2014).
16. W. Blondel, A. Delconte, G. Khairallah, F. Marchal, A. Gavoille, and M. Amouroux, "Spatially-resolved multiply-excited autofluorescence and diffuse reflectance spectroscopy: spectrolive medical device for skin in vivo optical biopsy," *Electronics* **10**(3), 243 (2021).
17. E. Torti, R. Leon, M. La Salvia, G. Florimbi, B. Martinez-Vega, H. Fabelo, S. Ortega, G. M. Callicó, and F. Leporati, "Parallel classification pipelines for skin cancer detection exploiting hyperspectral imaging on hybrid systems," *Electronics* **9**(9), 1503 (2020).
18. S. Heuke, N. Vogler, T. Meyer, D. Akimov, F. Kluschke, H. J. Rowert-Huber, J. Lademann, B. Dietzek, and J. Popp, "Detection and discrimination of non-melanoma skin cancer by multimodal imaging," *Healthcare* **1**(1), 64–83 (2013).
19. S. L. Wong, M. B. Faries, E. B. Kennedy, S. S. Agarwala, T. J. Akhurst, C. Ariyan, C. M. Balch, B. S. Berman, A. Cochran, K. A. Delman, M. Gorman, J. M. Kirkwood, M. D. Moncrieff, J. S. Zager, and G. H. Lyman, "Sentinel lymph node biopsy and management of regional lymph nodes in melanoma: American Society of Clinical Oncology and Society of Surgical Oncology clinical practice guideline update," *J Clin Oncol* **36**(4), 399–413 (2018).
20. A. B. E. Attia, S. Y. Chuah, D. Razansky, C. J. H. Ho, P. Malempati, U. S. Dinis, R. Bi, C. Y. Fu, S. J. Ford, J. S. Lee, M. W. P. Tan, M. Olivo, and S. T. G. Thng, "Noninvasive real-time characterization of non-melanoma skin cancers with handheld optoacoustic probes," *Photoacoustics* **7**, 20–26 (2017).
21. I. Steinberg, D. M. Huland, O. Vermesh, H. E. Frostig, W. S. Tummers, and S. S. Gambhir, "Photoacoustic clinical imaging," *Photoacoustics* **14**, 77–98 (2019).
22. J. Malvehy and G. Pellacani, "Dermoscopy, confocal microscopy and other non-invasive tools for the diagnosis of non-melanoma skin cancers and other skin conditions," *Acta Derm Venereol* **218**, 22–30 (2017).

23. L. Smith and S. Macneil, "State of the art in non-invasive imaging of cutaneous melanoma," *Skin Res Technol* **17**(3), 257–269 (2011).
24. C. Kim, T. N. Erpelding, L. Jankovic, M. D. Pashley, and L. V. Wang, "Deeply penetrating in vivo photoacoustic imaging using a clinical ultrasound array system," *Biomed Opt Express* **1**(1), 278–284 (2010).
25. L. Lin, P. Hu, J. Shi, C. M. Appleton, K. Maslov, L. Li, R. Zhang, and L. V. Wang, "Single-breath-hold photoacoustic computed tomography of the breast," *Nat Commun* **9**(1), 2352 (2018).
26. J. Yao and L. V. Wang, "Photoacoustic tomography: fundamentals, advances and prospects," *Contrast Media Mol Imaging* **6**(5), 332–345 (2011).
27. J. T. Oh, M. L. Li, H. F. Zhang, K. Maslov, G. Stoica, and L. V. Wang, "Three-dimensional imaging of skin melanoma in vivo by dual-wavelength photoacoustic microscopy," *J. Biomed. Opt* **11**(3), 034032 (2006).
28. Y. Wang, D. Xu, S. Yang, and D. Xing, "Toward in vivo biopsy of melanoma based on photoacoustic and ultrasound dual imaging with an integrated detector," *Biomed Opt Express* **7**(2), 279–286 (2016).
29. Y. Zhou, W. Xing, K. I. Maslov, L. A. Cornelius, and L. V. Wang, "Handheld photoacoustic microscopy to detect melanoma depth in vivo," *Opt. Lett.* **39**(16), 4731–4734 (2014).
30. A. Breathnach, E. Concannon, J. J. Dorairaj, S. Shaharan, J. McGrath, J. Jose, J. L. Kelly, and M. J. Leahy, "Preoperative measurement of cutaneous melanoma and nevi thickness with photoacoustic imaging," *J Med Imaging* **5**, 015004 (2018).
31. B. Aedán, C. Liz, A. Laura, D. Jemima, M. S. Hrehash, K. Jack, and J. L. Martin, "Assessment of cutaneous melanoma and pigmented skin lesions with photoacoustic imaging," in *Proc.SPIE*, (2015),
32. Y. Zhou, S. V. Tripathi, I. Rosman, J. Ma, P. Hai, G. P. Linette, M. L. Council, R. C. Fields, L. V. Wang, and L. A. Cornelius, "Noninvasive determination of melanoma depth using a handheld photoacoustic probe," *J Invest Dermatol* **137**(6), 1370–1372 (2017).
33. K. S. Valluru, K. E. Wilson, and J. K. Willmann, "Photoacoustic imaging in oncology: translational preclinical and early clinical experience," *Radiology* **280**(2), 332–349 (2016).
34. J. Kim, Y. H. Kim, B. Park, H. M. Seo, C. H. Bang, G. S. Park, Y. M. Park, J. W. Rhie, J. H. Lee, and C. Kim, "Multispectral ex vivo photoacoustic imaging of cutaneous melanoma for better selection of the excision margin," *Br J Dermatol* **179**(3), 780–782 (2018).
35. S. Y. Chuah, A. B. Attia, V. Long, C. J. Ho, P. Malempati, C. Y. Fu, S. J. Ford, J. S. Lee, W. P. Tan, D. Razansky, M. Olivo, and S. Thng, "Structural and functional 3D mapping of skin tumours with non-invasive multispectral optoacoustic tomography," *Skin Res Technol* **23**(2), 221–226 (2017).
36. S. Y. Chuah, A. B. E. Attia, C. J. H. Ho, X. Li, J. S. Lee, M. W. P. Tan, A. A. Yong, A. W. M. Tan, D. Razansky, M. Olivo, and S. T. G. Thng, "Volumetric Multispectral optoacoustic tomography for 3-dimensional reconstruction of skin tumors: a further evaluation with histopathologic correlation," *J Invest Dermatol* **139**(2), 481–485 (2019).
37. U. Dahlstrand, R. Sheikh, and M. Malmjö, "Photoacoustic imaging for intraoperative micrographic control of the surgical margins of eyelid tumours," *Acta Ophthalmol* **98**(2), e264–e265 (2020).
38. J. Hult, U. Dahlstrand, A. Merdasa, K. Wickerstrom, R. Chakari, B. Persson, M. Cinthio, T. Erlov, J. Albinsson, B. Gesslein, R. Sheikh, and M. Malmjö, "Unique spectral signature of human cutaneous squamous cell carcinoma by photoacoustic imaging," *J Biophotonics* **13**(5), e201960212 (2020).
39. S. L. Jacques, "Corrigendum: Optical properties of biological tissues: a review," *Physics in Medicine and Biology* **58**(14), 5007–5008 (2013).
40. A. Merdasa, J. Bunke, M. Naumovska, J. Albinsson, T. Erlöv, M. Cinthio, N. Reistad, R. Sheikh, and M. Malmjö, "Photoacoustic imaging of the spatial distribution of oxygen saturation in an ischemia-reperfusion model in humans," *Biomed Opt Express* (in press).
41. S. Konugolu Venkata Sekar, J. S. Beh, A. Farina, A. Dalla Mora, A. Pifferi, and P. Taroni, "Broadband diffuse optical characterization of elastin for biomedical applications," *Biophys Chem* **229**, 130–134 (2017).
42. B. Cox, J. G. Laufer, S. R. Arridge, and P. C. Beard, "Quantitative spectroscopic photoacoustic imaging: a review," *J. Biomed. Opt* **17**(6), 061202 (2012).
43. D. K. Yao, C. Zhang, K. Maslov, and L. V. Wang, "Photoacoustic measurement of the Gruneisen parameter of tissue," *J. Biomed. Opt* **19**(1), 017007 (2014).
44. R. Sheikh, M. Cinthio, U. Dahlstrand, T. Erlov, M. Naumovska, B. Hammar, S. Zackrisson, T. Jansson, N. Reistad, and M. Malmjö, "Clinical translation of a novel photoacoustic imaging system for examining the temporal artery," *IEEE Trans Ultrason Ferroelectr Freq Control* **66**(3), 472–480 (2019).
45. IEC, "Safety of laser products – Part 1: Equipment classification and requirements," in *International Standard IEC 60825-1*, (2014).
46. FDA, "Information for Manufacturers Seeking Marketing Clearance of Diagnostic Ultrasound Systems and Transducers," in *Guidance for Industry and FDA Staff*, U. S. D. o. H. a. H. Services, ed. (Food and Drug Administration, 2008).
47. BMUS, "Guidelines for the safe use of diagnostic ultrasound equipment," (The British Medical Ultrasound Society, 2010).
48. B. Park, C. H. Bang, C. Lee, J. H. Han, W. Choi, J. Kim, G. S. Park, J. W. Rhie, J. H. Lee, and C. Kim, "3D wide-field multispectral photoacoustic imaging of human melanomas in vivo: a pilot study," *J Eur Acad Dermatol Venereol* **35**(3), 669–676 (2021).

49. J. Hult, A. Merdasa, A. Pekar-Lukacs, M. Tordengren Stridh, A. Khodaverdi, J. Albinsson, B. Gesslein, U. Dahlstrand, L. Engqvist, Y. Hamid, D. Larsson Alber, B. Persson, T. Erlov, R. Sheikh, M. Cinthio, and M. Malmjö, "Comparison of photoacoustic imaging and histopathological examination in determining the dimensions of 52 human melanomas and nevi ex vivo," *Biomed Opt Express* **12**(7), 4097–4114 (2021).
50. N. C. Zeitouni, D. J. Rohrbach, M. Aksahin, and U. Sunar, "Preoperative ultrasound and photoacoustic imaging of nonmelanoma skin cancers," *Dermatol Surg* **41**(4), 525–528 (2015).
51. H. M. Gloster Jr. and K. Neal, "Skin cancer in skin of color," *J Am Acad Dermatol* **55**(5), 741–760 (2006).
52. P. Liu, Z. Zhu, C. Zeng, and G. Nie, "Specific absorption spectra of hemoglobin at different PO₂ levels: potential noninvasive method to detect pO₂ in tissues," *J. Biomed. Opt* **17**(12), 125002 (2012).
53. M. Lupu, C. Caruntu, M. I. Popa, V. M. Voiculescu, S. Zurac, and D. Boda, "Vascular patterns in basal cell carcinoma: Dermoscopic, confocal and histopathological perspectives," *Oncol Lett* **17**, 4112–4125 (2019).
54. K. Sellheyer, "Basal cell carcinoma: cell of origin, cancer stem cell hypothesis and stem cell markers," *Br J Dermatol* **164**(4), 696–711 (2011).
55. K. Thieu, M. E. Ruiz, and D. M. Owens, "Cells of origin and tumor-initiating cells for nonmelanoma skin cancers," *Cancer Letters* **338**(1), 82–88 (2013).
56. E. Alessi, L. Venegoni, D. Fanoni, and E. Berti, "Cytokeratin profile in basal cell carcinoma," *Am J Dermatopathol* **30**(3), 249–255 (2008).
57. K. P. Nielsen, Z. Lu, P. Juzenas, J. J. Stamnes, K. Stamnes, and J. Moan, "Reflectance spectra of pigmented and nonpigmented skin in the UV spectral region," *Photochem Photobiol* **80**(3), 450–455 (2004).
58. M. Seiberg, "Keratinocyte-melanocyte interactions during melanosome transfer," *Pigment Cell Research* **14**(4), 236–242 (2001).
59. R. Sheikh, B. Hammar, M. Naumovska, U. Dahlstrand, B. Gesslein, T. Erlov, M. Cinthio, and M. Malmjö, "Photoacoustic imaging for non-invasive examination of the healthy temporal artery - systematic evaluation of visual function in healthy subjects," *Acta Ophthalmol* **99**(2), 227–231 (2021).
60. T. Erlov, R. Sheikh, U. Dahlstrand, J. Albinsson, M. Malmjö, and M. Cinthio, "Regional motion correction for in vivo photoacoustic imaging in humans using interleaved ultrasound images," *Biomed Opt Express*, In press (2021).